

# Phosphonated graphene oxide-modified polyacrylamide hydrogel electrolytes for solid-state zinc-ion batteries

Ali Abbasi<sup>a,b</sup>, Yaolin Xu<sup>b,\*</sup>, Ebrahim Abouzari-Lotf<sup>c,d</sup>, Mohammad Etesami<sup>a</sup>, Ramin Khezri<sup>a</sup>, Sebastian Risse<sup>b</sup>, Nikolay Kardjilov<sup>e</sup>, Khanh Van Tran<sup>e</sup>, Haojun Jia<sup>f</sup>, Anongnat Somwangthanaroj<sup>a,i</sup>, Ingo Manke<sup>e</sup>, Yan Lu<sup>b,g,\*</sup>, Soorathep Kheawhom<sup>a,h,i,\*\*</sup>

<sup>a</sup> Department of Chemical Engineering, Faculty of Engineering, Chulalongkorn University, Bangkok 10330, Thailand

<sup>b</sup> Department for Electrochemical Energy Storage, Helmholtz-Zentrum Berlin für Materialien und Energie, Hahn-Meitner-Platz 1, Berlin, Germany

<sup>c</sup> Helmholtz Institute Ulm (HIU), Helmholtzstraße 11, Ulm 89081, Germany

<sup>d</sup> Institute of Nanotechnology, Karlsruhe Institute of Technology, P.O. Box 3640, Karlsruhe 76021, Germany

<sup>e</sup> Institute Applied Materials, Helmholtz-Zentrum Berlin für Materialien und Energie, Hahn-Meitner-Platz 1, Berlin, Germany

<sup>f</sup> Department of Chemistry, Massachusetts Institute of Technology, Cambridge, MA 02139, USA

<sup>g</sup> Institute of Chemistry, University of Potsdam, Potsdam, Germany

<sup>h</sup> Center of Excellence on Advanced Materials for Energy Storage, Chulalongkorn University, Bangkok 10330, Thailand

<sup>i</sup> Bio-Circular-Green-economy Technology & Engineering Center (BCGeTEC) Faculty of Engineering, Chulalongkorn University, Bangkok 10330, Thailand

## ARTICLE INFO

### Keywords:

Gel polymer electrolyte  
Manganese oxide  
Flexible battery  
Hydrogen bound  
X-ray tomography

## ABSTRACT

Compared to rigid batteries using liquid electrolytes, solid-state batteries (SSBs) offer several advantages: flexibility, prevention of leakage, suppression of dendritic formation and hydrogen evolution, as well as minimization of cathode active material dissolution. For the materialization of real-life SSBs, gel polymer electrolytes (GPEs) are among promising candidates. However, development of GPEs with satisfying ionic conductivity and mechanical endurance is challenging. Herein, we report on the development of polyacrylamide (PAM)/phosphonated graphene oxide (PGO) nanocomposite hydrogel electrolytes for zinc-ion batteries; PGO acts as the filler through in-situ polymerization of acrylamide in an aqueous suspension of PGO. The synthesized PAM/PGO hydrogel exhibits high ionic conductivity of 31.0 mS/cm at 30 °C compared to that of PAM (13.8 mS/cm) and PAM-GO (20.8 mS/cm). The higher ionic conductivity of PAM-PGO can be attributed to its higher hydrophilicity and electrolyte storage capacity along with its lower activation energy for ionic conduction (7.2 KJ/mol K) in comparison with that of PAM (10.1 KJ/mol K) and PAM-GO (10.2 KJ/mol K). The interaction between water against PAM, PAM-GO and PAM-PGO is investigated via density-functional theory (DFT). The MnO<sub>2</sub>-based zinc-ion battery assembled using PAM-PGO as electrolyte shows high initial capacity of 240 mAh/g, losing only 4 and 15% of its capacity after 100 and 145 cycles, respectively. Results demonstrate promising potential of PAM-PGO as a solid-state electrolyte for flexible battery applications.

## 1. Introduction

Zinc-ion batteries (ZIBs) are promising alternatives for lithium-ion batteries (LIBs) because of their low cost, high energy density, safety and high theoretical capacity (820 mAh/g and 5855 mAh/cm<sup>3</sup>) as well as easy assembly under ambient condition [1–3]. Even though liquid electrolytes offer high ionic conductivity, their application is limited. It is seen that liquid electrolytes can leak under strain, and limit the

flexibility of ZIBs; dendritic formation also leads to short circuits [4,5]. Due to irreversible side reactions, ZIBs suffer from fast capacity decay and poor cycling performance.

As a substitute to replace aqueous electrolytes, GPEs are seen as potential candidates. In GPEs, a polymeric framework absorbs a solution of zinc salts and a gel is formed. The absence of free water molecules in GPEs results in several advantages for ZIBs. The risk of electrolyte leakage does not exist anymore, affording high flexibility for ZIBs using

\* Corresponding authors at: Department for Electrochemical Energy Storage, Helmholtz-Zentrum Berlin für Materialien und Energie, Hahn-Meitner-Platz 1, Berlin, Germany.

\*\* Corresponding author at: Department of Chemical Engineering, Faculty of Engineering, Chulalongkorn University, Bangkok 10330, Thailand.

E-mail addresses: [yaolin.xu@helmholtz-berlin.de](mailto:yaolin.xu@helmholtz-berlin.de) (Y. Xu), [yan.lu@helmholtz-berlin.de](mailto:yan.lu@helmholtz-berlin.de) (Y. Lu), [soorathep.k@chula.ac.th](mailto:soorathep.k@chula.ac.th) (S. Kheawhom).

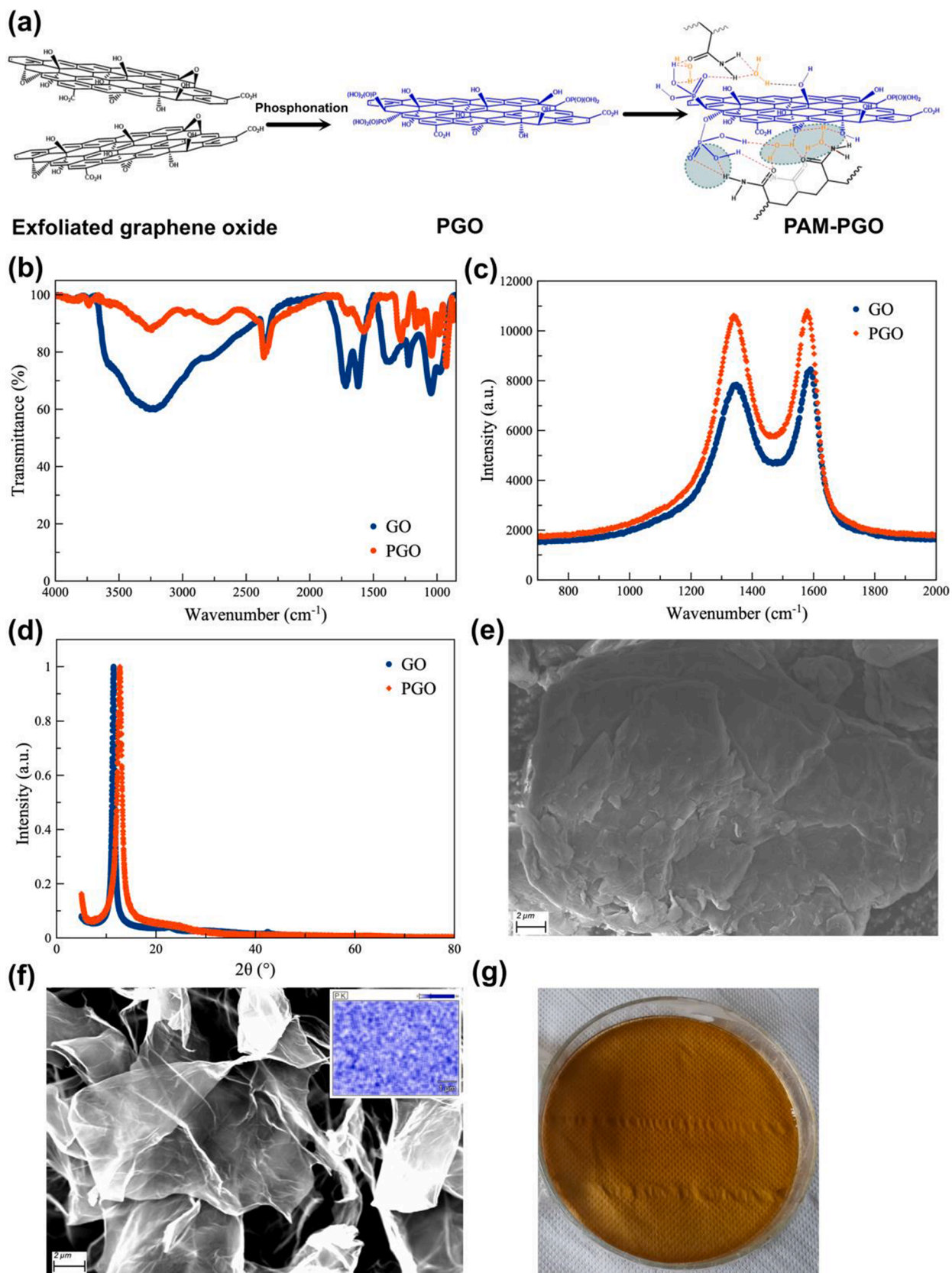


**Fig. 1.** (a) Schematic view of GO phosphonation reaction and PAM-PGO structure showing hydrogen bonds, (b) FTIR, (c) Raman, and (d) XRD spectra of GO and PGO; SEM images of (e) GO and (f) PGO, and (g) Photo of PAM-PGO film.

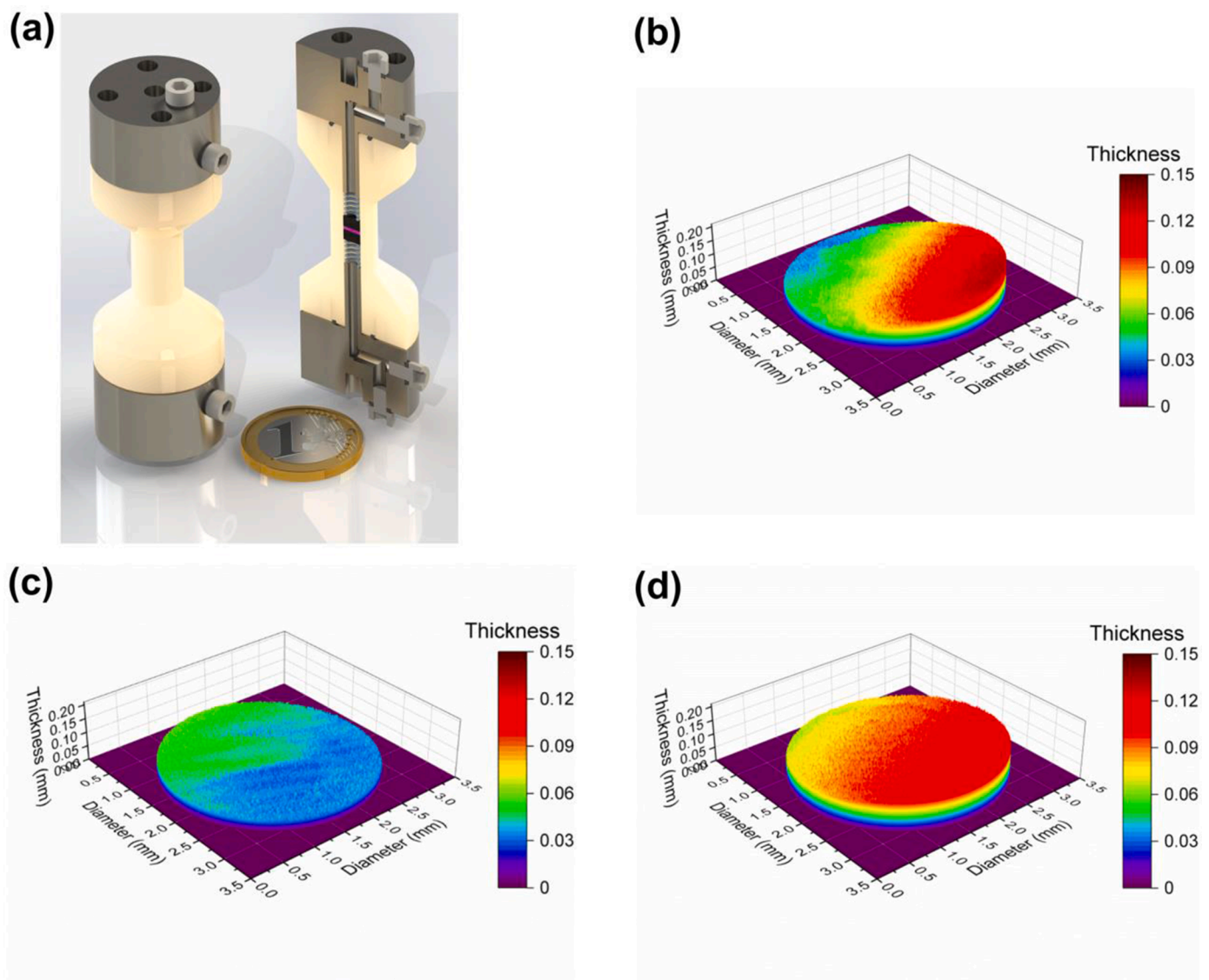


Fig. 2. (a) In-house designed cell for EIS with high transparency against X-ray, (b) 3D tomograph of PAM, (c) 3D tomograph of PAM-GO, and (d) 3D tomograph of PAM-PGO.

GPEs. Furthermore, hydrogen evolution reaction (HER), which is a critical issue in aqueous electrolytes is reduced dramatically, resulting in higher coulombic efficiency and higher cycling stability. When GPEs are applied, dendritic formation is prevented owing to the coverage of newly formed dendrites by gel material, preventing their further growth [6]. Besides, dissolution of cathode active material is impeded and there is no need to use a separator in the battery [4].

Gelatin [7], polyvinyl alcohol (PVA) [8], polyacrylic acid (PAA) [9], and PAM [10] are among several types of polymers that have been used as GPEs in ZIBs. Of them, PAM is very promising on account of its structural properties [11]. Almost all PAM chain segments are connected through cross-linking, offering better mechanical properties than other GPEs, such as PVA. Moreover, through the presence of hydrophilic functional groups (especially amide groups), PAM-based GPEs can trap enough aqueous solutions containing zinc ions in its structure, leading to high ionic conductivity [4]. However, state-of-the-art PAM-based GPEs are of low ionic conductivity around 17 mS/cm [10]. By increasing the electrolyte content of PAM hydrogels, their ionic conductivity can be improved, but such action can lead to a significant decrease in their mechanical properties [12]. To overcome these problems, various approaches including grafting PAM onto other polymers such as gelatin

[13] (17.6 mS/cm at room temperature) and nanofibrillated cellulose [12] (22.8 mS/cm at room temperature) or using different additives such as graphene oxide (GO) [4] (20 mS/cm at 20 °C) have been reported. Even though these methods have improved various properties of PAM-based GPEs such as mechanical properties [12] or low-temperature performance [4], yet higher ionic conductivity with better mechanical strength is required for developing efficient zinc-ion batteries.

To solve this problem, more conductive electrolyte additives have been used. Certain additives can improve ionic conductivity by augmenting the type and number of conductive ions utilized e.g.  $Mn^{2+}$  additive [14] and  $Na^+$  additive [15] etc. Thus, the electrochemical window is broadened by suppressing the oxygen evolution reaction (OER) and hydrogen evolution reaction (HER) through the application of sodium dodecyl sulfate (SDS) [16] and citric acid [17]. In general, improving the ionic conductivity of GPEs is demanding; so hydrogels with high mechanical properties and ionic conductivity at the same time remain exacting [18]. The introduction of acid functionality in the gel matrix has been proposed as an efficient strategy to concurrently improve the ionic conductivity and mechanical properties of GPEs. Hydrogen bonds between the acidic group, water and the main gel

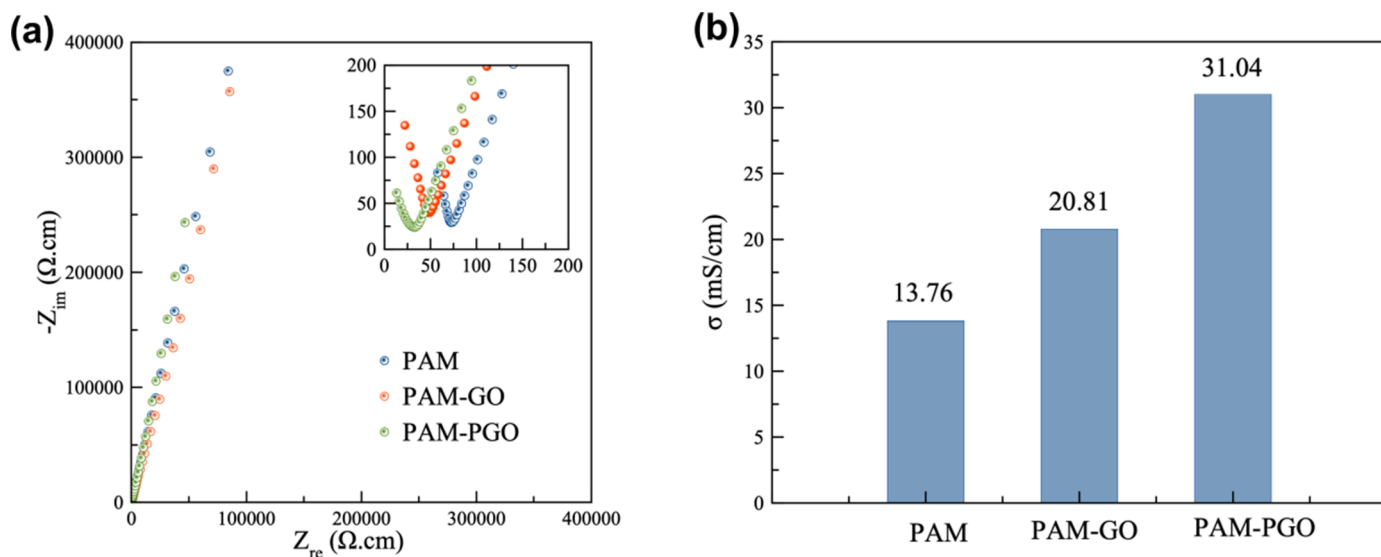


Fig. 3. (a) Nyquist plots of PAM, PAM-GO, and PAM-PGO at 30 °C (Insert: high frequency area), and (b) their ionic conductivity.

backbone can effectively retain the water in the gel matrix, guaranteeing excellent water retaining ability. Hydrogen bonds can simultaneously ensure mechanical stability under high stress repeated tensile deformation [19].

PGO, a derivative of graphene oxide synthesized by introducing phosphonic acid functional groups into its structure, has been investigated and is seen to improve the ionic conductivity of Nafion up to 40% [20], polyvinylidene fluoride PVDF [21], and polybenzimidazole [22]. It is significant that the incorporation of PGO can raise the tensile strength of resulting polymers without a considerable decline in the elongation at break of the resulting polymers. This is due to the amphoteric character of phosphonic acid, its ability to form stronger hydrogen bonds to retain water whilst upholding the excellent mechanical properties of the GO sheet [22].

In this work, we have designed and developed new PAM-based GPEs consisting of PAM as the gel-forming polymer, PGO nanosheets as additives, and an electrolyte solution containing zinc-sulfate and manganese sulfate. It is noted that phosphonic acid in PGO improves ionic conductivity by functioning as a network to retain the water in the gel structure; graphene serves as the mechanical support. In addition, the acid functionality of GO enhances its dispersion and improves gel-additive compatibility. X-ray tomography has been used for the first time to accurately measure the gel thickness inside the tomography cell for EIS measurement. As a result, more accurate calculation of ionic conductivity has been possible. Developed GPEs possess higher ionic conductivity (31.0  $\text{mS/cm}$ ) than that of pristine PAM (13.8  $\text{mS/cm}$ ) and GO modified PAM (20.8  $\text{mS/cm}$ ). The PGO-modified PAM GPE has high potential to be used in various high-performance aqueous batteries and other energy storage devices such as fuel cells.

## 2. Experimental

### 2.1. Materials

Potassium persulfate (KPS) ( $\geq 99.5\%$ ), and N,N'-methylenebis (acrylamide) (BIS) (99%), phosphoric acid (PA) ( $\geq 85$  wt% in water), polyphosphoric acid (PPA) (115%  $\text{H}_3\text{PO}_4$  basis) and zinc sulfate heptahydrate ( $\geq 99\%$ ) were purchased from Sigma-Aldrich. Acrylamide (Sigma,  $\geq 99\%$ ) was used without further purification. Manganese (II) sulfate monohydrate ( $>99\%$ ) was supplied by Acros Organics. For PGO purification, dialysis tubing, also known as Visking tubing, (Carl Roth GmbH+Co., type 36/32 inch, thickness: 0.02 mm, W: 44 mm) was used. Carbon paper (Ion Power, SIGRACET® GDL 29 AA) was used for cathode

preparation. GO powder ( $< 35$  mesh) was purchased from Abalonyx AS.

### 2.2. Synthesis of phosphonated graphene oxide (PGO)

For PGO synthesis, a modified version of the previously reported method [23,24] was used. Sonication was used to homogenize a mixture of PPA (1.5 g) and PA (7.5 g) i.e. 9 g and 1:5 wt.%; pH solution was adjusted to 5 using 0.4 M sodium hydroxide solution. The solution was poured into a 500 ml 3-necked flask along with 50 mL of GO in deionized (DI) water (0.5 wt.%): 0.25 g GO sonicated for 30 min was added under continuous stirring. The mixture was heated to 95 °C and stirred under reflux conditions for 8 h. The highly dispersed PGO was precipitated by an ultra-high-speed centrifuge (at 9500 rpm) at 2 °C and washed a few times with DI water. For further purification of the synthesized PGO, the centrifuged particles were dispersed in DI water and poured into a dialysis tubing. The tubing was floated in a 5 L beaker filled with DI water. The water was changed every 12 h until its conductivity was negligible to make sure all the dissolved molecules were extracted from the PGO dispersion. Finally, the dispersion was freeze-dried overnight, and a foam-like precipitate was collected as pure PGO.

### 2.3. Preparation of PGO-PAM hydrogel electrolyte

0.01 g (1 wt% of polymer) PGO was added to 6 ml DI water in flask (No. 1) and ultrasonicated for 1 h. Then, 1 g acrylamide was dissolved in the dispersion while bubbling with  $\text{N}_2$ . For the next stage, the mixture was ultrasonicated for 40 min to make sure of uniform dispersion of PGO particles in the monomer solution. While ultrasonating the mixture in flask No. 1, 4 ml DI water was bubbled with nitrogen gas for 5 min in another flask (No. 2) at ice water temperature. Both 3 mg BIS (cross-linker) and 10 mg KPS (initiator) were added and stirred under  $\text{N}_2$  for 10 min until dissolved. The content of flask No. 2 (initiator and cross-linker solution) was added to flask No. 1 (polymer and PGO dispersion, after the last ultrasonication stage) while stirring. Then, the mixture was transferred to a home-made casting mold and placed in an oven at 60 °C for about 2 h. Subsequently, a thin composite hydrogel with the thickness of 0.5 mm was formed. Finally, small pieces of the gel were soaked in the electrolyte solution ( $\text{ZnSO}_4$ , 2M +  $\text{MnSO}_4$ , 0.1M). The same method was used to prepare PAM-GO and pure PAM hydrogels for comparison.

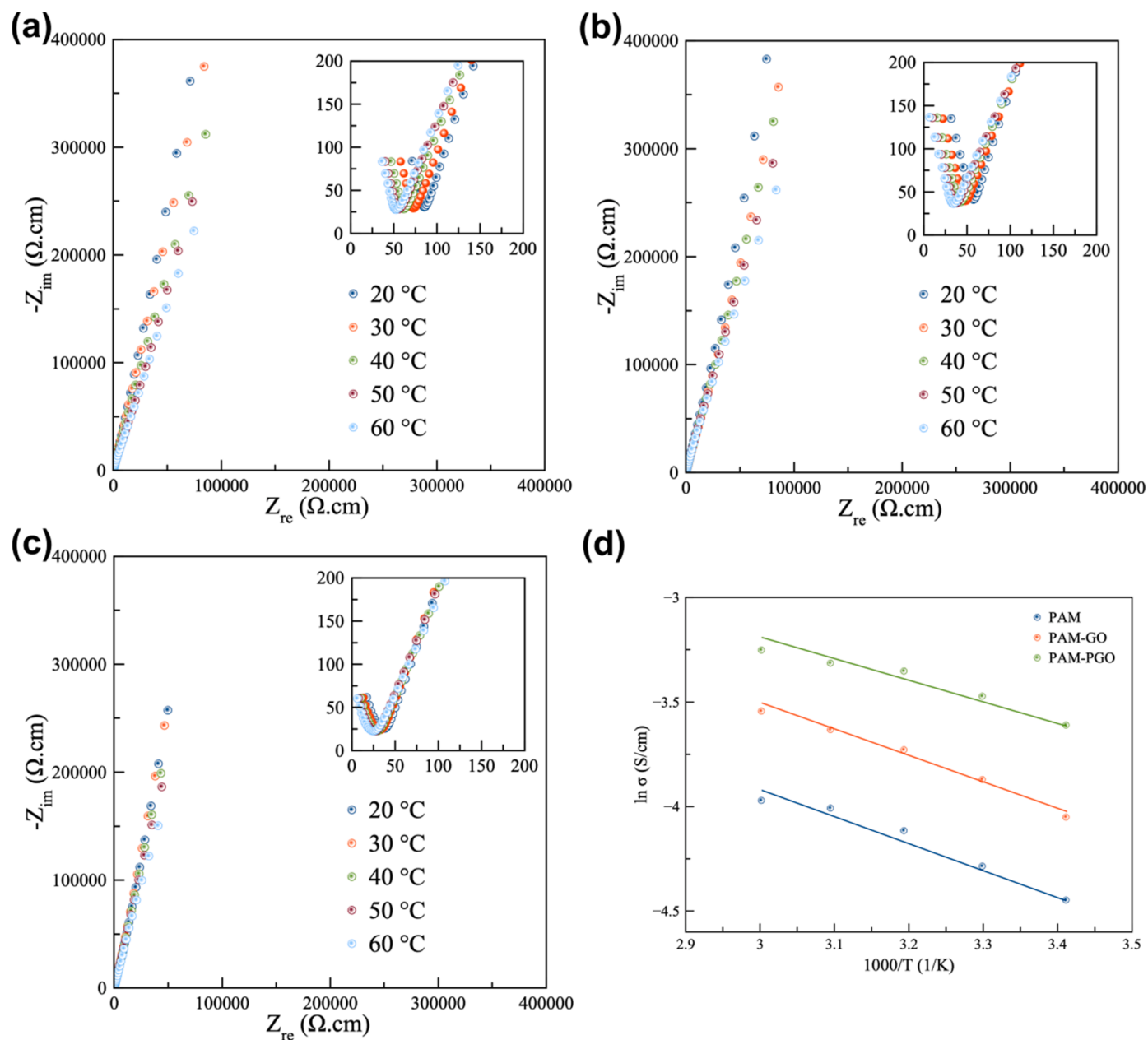


**Fig. 4.** Nyquist plots of (a) PAM, (b) PAM-GO, (c) PAM-PGO at various temperatures in the range of 20-60 °C (Inserts: high frequency area), and (d) Arrhenius plots of the logarithm of conductivity versus inverse of temperature for PAM, PAM-GO, and PAM-PGO.

#### 2.4. Synthesis of $\alpha$ -MnO<sub>2</sub> and cathode preparation

$\alpha$ -MnO<sub>2</sub> was synthesized using a previously reported hydrothermal method [25]. Thus, both 1 mmol KMnO<sub>4</sub> and 1.5 mmol MnSO<sub>4</sub> were dissolved in 20 mL DI water and placed in an autoclave reactor at 120 °C for 3 h. The synthesized  $\alpha$ -MnO<sub>2</sub> precipitate was washed with DI water, dried at 80 °C, and ground into fine particles. The morphology and the XRD pattern of the  $\alpha$ -MnO<sub>2</sub> synthesized are shown in Fig. S1. For preparation of the cathode, synthesized  $\alpha$ -MnO<sub>2</sub> was mixed with super-carbon black and PVDF having a weight ratio of 7:2:1 in N-methyl pyrrolidone (NMP). The slurry was then coated onto carbon paper and dried at 60 °C overnight. The mass loading of  $\alpha$ -MnO<sub>2</sub> onto the cathode was in the range: 1-1.5 mg/cm<sup>2</sup>.

#### 2.5. X-ray tomography and data analysis

##### 2.5.1. Micro X-ray tomography

X-ray imaging is a non-destructive method used widely in the investigation of material science and engineering [26]. The in-house X-ray imaging device built at Helmholtz-Zentrum Berlin consisted of an X-ray tube (Hamamatsu, L8121-03) and a flat panel detector (Hamamatsu, C7942SK-05). The instrument allows for changing the field of view and the spatial resolution by adjusting the source-detector distance and source-object distance. The facility is set up to produce a cone beam from the micro focus X-ray source.

In this study, three tomographies of PAM, PAM-GO and PAM-PGO cells were implemented using the X-ray tube voltage of 60 kV and current of 166  $\mu$ A as well as the source-to-sample and source-to-detector distances of 58 and 400 mm, respectively. The experiments were measured via the rotation of 360° through 1000 projections with an exposure time of 1.2 s and 3 frames. The resolution achieved from these

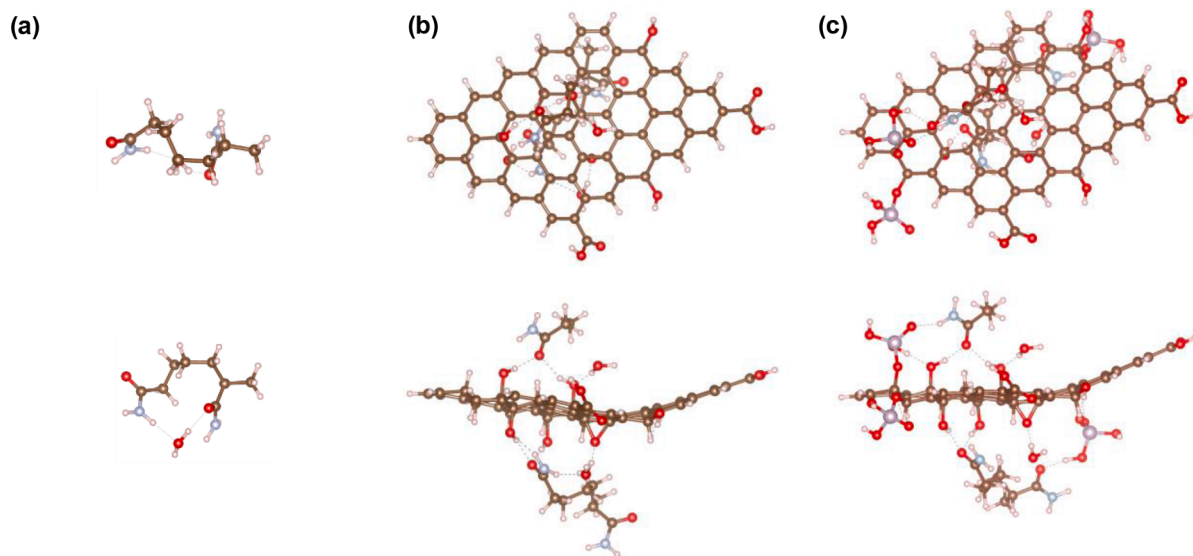


**Fig. 5.** Top and side views of the optimized structures of the repeating unit ( $-\text{CH}_2\text{CHCONH}_2-$ ) of (a) PAM, (b) PAM-GO and (c) PAM-PGO interacting with  $\text{H}_2\text{O}$  molecules. Brown, white, silver, red and purple spheres represent carbon, hydrogen, nitrogen, oxygen and phosphorus atoms, respectively.

experiments proved to be  $7.175 \mu\text{m}/\text{voxel}$ .

### 2.5.2. Data processing

The principle of the X-ray tomographic imaging method is based on different X-ray attenuation coefficients of different materials. Thus, samples were located between the X-ray source and detector to record their transmission images. The obtained datasets were then normalized using darkfields and flatfields via the reconstruction software: Octopus [27]. After normalization, datasets were reconstructed using filtered back projection. The calculation of the thickness of the gel layers is based on the difference in the X-ray attenuation coefficients between the gel and electrode materials. A mathematical algorithm was applied. Firstly, the derivative of the attenuation profiles was taken. Secondly, the thickness of the gel was calculated. Both applications used IDL 8.2. Finally, the 3D distribution of thickness was implemented via the software: Origin.

### 2.6. Cell assembly and electrochemical tests

All electrochemical tests were carried out using coin cell CR2025 unless mentioned otherwise. Consequently, the gels were sandwiched between the  $\text{MnO}_2$ -loaded carbon paper cathode and the metallic zinc film anode. Two stainless steel spacers along with a spring were used to ensure a suitable connection for the coin cell components. For coin cell assembly, a digital pressure-controlled electric crimper (MTI Corporation, MSK-106) was used to apply uniform pressure for all the assembled cells. Electrochemical impedance spectroscopy (EIS) was performed in the frequency range of 1 Hz - 1 MHz at room temperature using a Gamry Model Potentiostat/Galvanostat with EIS unit. Cyclic voltammetry (CV) was performed using Gamry Model Potentiostat/Galvanostat. Galvanostatic charge/discharge (GCD) measurements were carried out using an Arbin Model battery testing system.

### 2.7. Characterization

Morphological properties of the samples and their surface chemistry were investigated using scanning electron microscope (SEM LEO GEMINI 1530) equipped with an energy dispersive X-ray (EDS) detector (Thermo Fischer). To evaluate the crystalline structure, X-ray diffraction (XRD: Bruker D8) was carried out. The chemical structure of the samples was analyzed using a confocal Raman microscope (Alpha 300, WITec, Ulm, Germany; excitation wavelength: 532 nm; integration time: 60 s;

plus CCD detector: DU401A-BV, UK), and Fourier transform infrared spectroscopy (FTIR: Perkins Elmer with a diamond Cristal and ATR mode).

### 2.8. Density functional theory calculation

Gas-phase geometry optimizations were performed using density functional theory (DFT) with a developer version of the GPU-accelerated electronic structure code TeraChem v1.9 [28]. The range-separated hybrid functional B3LYP was employed for all calculations with the 6-31G\* basis. The default tolerances are  $4.5 \times 10^{-4}$  hartree/bohr for the maximum gradient, and  $1 \times 10^{-6}$  hartree for the change in self-consistent field (SCF) energy between steps.

The binding energies between the PAM, PAM-GO and PAM-PGO systems with water molecules were computed according to Eq. (1):

$$E_{\text{PAM-H}_2\text{Obinding}} = E_{\text{PAM+H}_2\text{O}} - E_{\text{PAM}} - E_{\text{H}_2\text{O}} \quad (1)$$

where  $E_{\text{PAM+H}_2\text{O}}$  is the energy of the modified PAM with water molecules,  $E_{\text{PAM}}$  is the energy of PAM, and  $E_{\text{H}_2\text{O}}$  is the energy of water molecule in gas phase.

Similarly, the binding energies between the modified graphene oxide flakes with water molecules were computed according to Eq. (2):

$$E_{\text{GO-H}_2\text{Obinding}} = E_{\text{GO+H}_2\text{O}} - E_{\text{GO}} - E_{\text{H}_2\text{O}} \quad (2)$$

where  $E_{\text{GO+H}_2\text{O}}$  is the energy of the modified graphene oxide flake with water molecules,  $E_{\text{GO}}$  is the energy of the modified graphene oxide flake.

## 3. Results and discussion

### 3.1. Structural analysis

Successful phosphonation of GO sheets was confirmed by FTIR and Raman spectroscopy. In Fig. 1a, a schematic view of the phosphonation reaction and the formation of several hydrogen bonds leading to better mechanical performance is depicted. Consequently, new peaks appeared in the FTIR spectrum, confirming the successful introduction of the phosphonic acid functional groups (Fig. 1b and Table S1). The peaks relating to P-Ar (Aromatic) and P-O-Ar reveal that P is connected to the GO structure through direct bonding with carbon via an oxygen bridge. In addition, the stretching peak of  $\text{C}=\text{O}$  is seen to shift from  $1573 \text{ cm}^{-1}$  for GO to around  $1616 \text{ cm}^{-1}$  for PGO. Stronger hydrogen bonds are

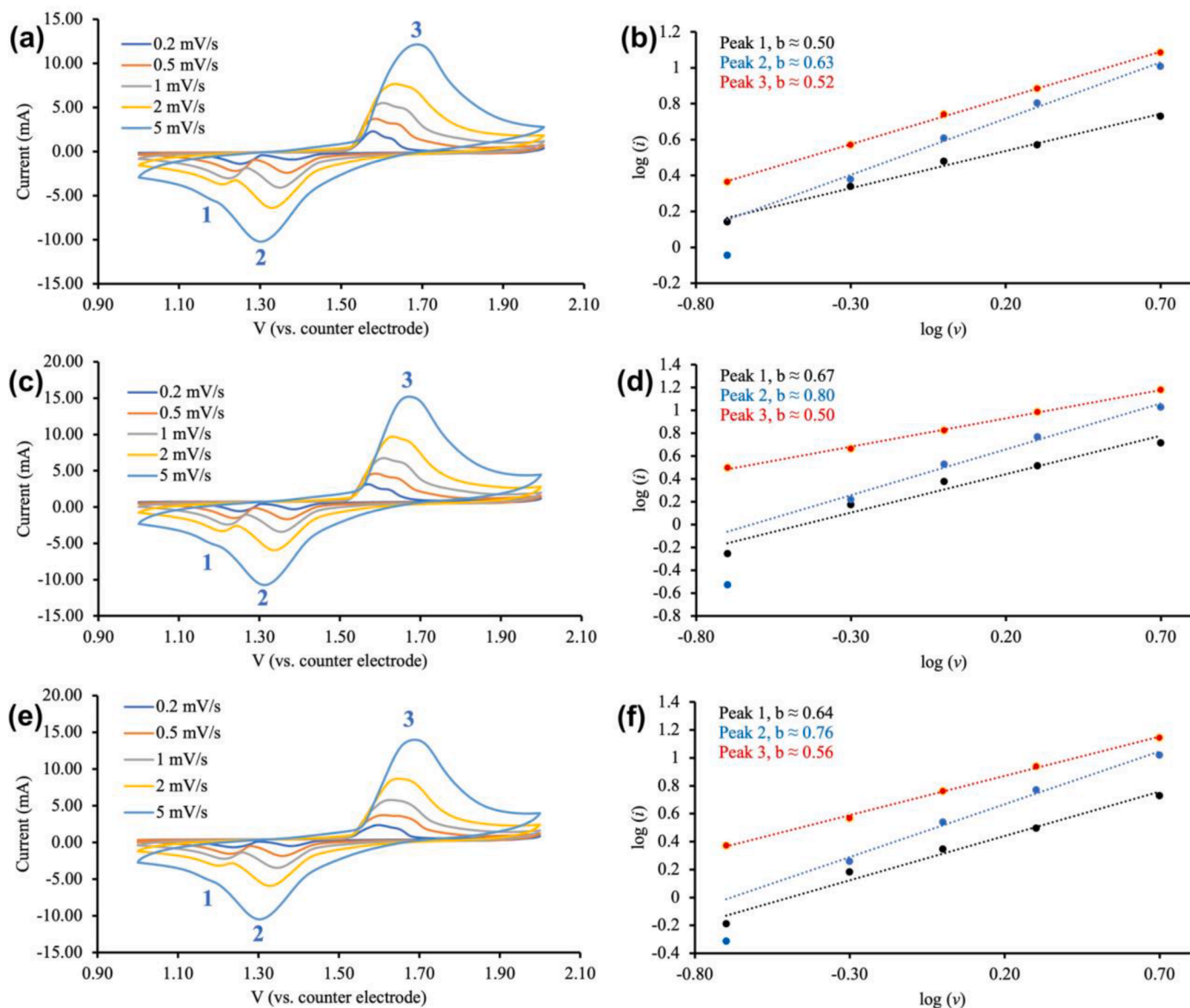


**Fig. 6.** Schema of CV curves: (a) PAM, (c) PAM-GO, and (e) PAM-PGO at various scan rates between 0.2 to 5 mV/s,  $\log(i)$  vs.  $\log(v)$  and  $b$  values for (b) PAM, (d) PAM-GO, and (f) PAM-PGO at peak currents: Peak 1 and Peak 2 extracted from CV.

formed because of less involvement of carboxylic acids compared to high involvement of phosphonic acid groups in the hydrogen bonds [29].

Fig. 1c shows the Raman spectra of GO and PGO. After phosphonation, the peaks at the G-band and D-band viz. 1591 and 1349 for GO shifted to 1579 and 1339 for PGO, respectively. Moreover, the ID/IG ratio increased from 0.93 for GO to 0.98 for PGO, confirming the structural change of GO upon phosphonation [29,30]. Increasing ID/IG ratio verifies the formation of large edges and defects on the structure of GO due to phosphonation [30].

After phosphonation, GO sheets are wrinkled and twisted. Such an outcome is ascribed to the introduction of phosphonic acid groups onto their surfaces (Fig. 1e and f). These functional groups can bind to each other on the same sheet or neighboring sheets through hydrogen bonds, resulting in the formation of wrinkles and twists. In Fig. 1f (inset image), EDX analysis of PGO confirms uniform functionalization on its surface. The strong interaction between the PGO sheets decreases the interlayer distance as verified via XRD analysis. GO shows a single peak at  $2\theta = 11.46^\circ$ , corresponding to an interlayer distance of 0.77 nm. After phosphonation, the peak moved to  $2\theta = 12.74^\circ$ , showing an interlayer

distance of 0.69 nm (Fig. 1d). Fig. 1g shows the photo of the PAM-PGO film.

### 3.2. Electrochemical characterization

#### 3.2.1. Ionic conductivity

An in-house designed cell with high transparency against X-ray was used to determine ionic conductivity (Fig. 2a). In this cell, circular pieces of the gel with a diameter of 3 mm and initial thickness of 500  $\mu\text{m}$  are sandwiched between two glassy carbon electrodes, which are pressed against the electrolyte by two springs. EIS measurement was carried out. Subsequently, 3D computed tomography (CT) was performed to accurately measure the gel thickness. This procedure was completed by measuring the thickness of the gel at each point of the gel. The effective gel thickness and the bulk resistance extracted from EIS were then used to calculate ionic conductivity. In Fig. 2b-d, 3-D X-Ray computed tomographies of PAM, PAM-GO and PAM-PGO gel structures inside the cell assembly are displayed.

Using X-ray tomography, the effective thickness of the PAM, PAM-GO, and PAM-PGO proved to be 74, 37, and 89  $\mu\text{m}$ , respectively. To

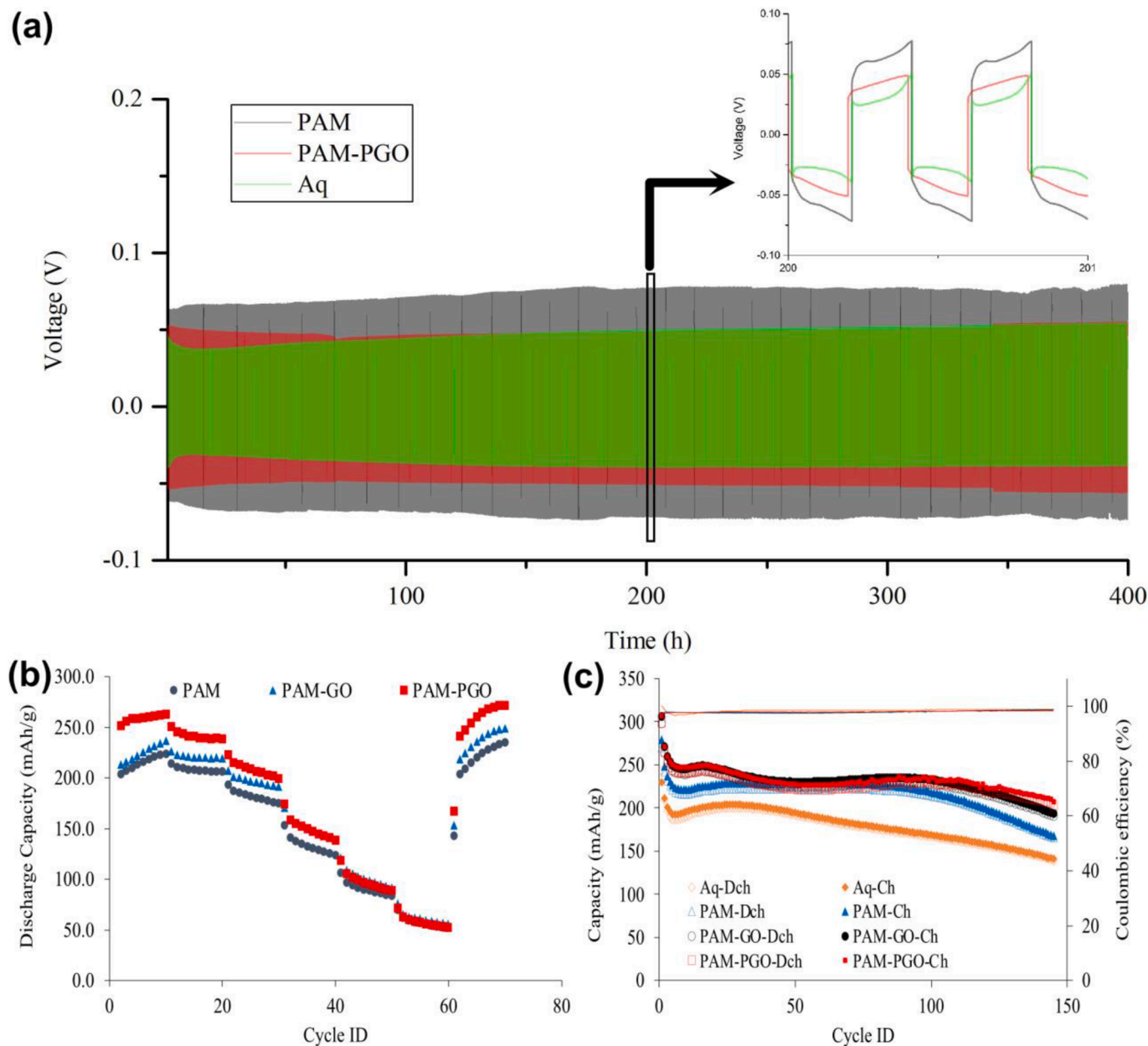


**Fig. 7.** (a) Cycling profile of Zn/GPE/Zn symmetric cells with PAM, PAM-PGO, and aqueous electrolytes at 0.25 mA/cm<sup>2</sup> up to 0.05 mAh/cm<sup>2</sup> for 1000 cycles, (b) Rate performance of ZIBs with PAM, PAM-GO, and PAM-PGO hydrogels as electrolytes at discharge current densities of 50, 100, 200, 500, 1000, 2000, and 50 mA/g, and (c) Cycling performance of Zn-MnO<sub>2</sub> battery at charge/discharge current density of 100 mA/g assembled using various electrolytes and their coulombic efficiency.

the best of our knowledge, this is the first time that X-ray tomography has been used in measuring ionic conductivity of GPEs attaining high accuracy. In Fig. 3, Nyquist plots and ionic conductivities of the prepared gels are shown. An animated video of the structure of the gel in the assembled cell is demonstrated in the supplementary document.

Bulk resistance of the assembled cells at high frequency at the intersection of the graph with the x-axis was used to measure ionic conductivity, as expressed in Eq. (3) [31]:

$$\sigma = l/R_b \cdot A \quad (3)$$

where  $\sigma$  is the ionic conductivity (S/cm),  $R_b$  is the bulk resistance ( $\Omega$ ), and  $l$  and  $A$  are thickness (cm) and area (cm<sup>2</sup>) of the gel, respectively. Ionic conductivity of PAM, PAM-GO, and PAM-PGO was found to be 13.8, 20.8, and 31.0 mS/cm, respectively. PAM-PGO exhibited the

highest ionic conductivity among PAM-based gel electrolytes previously reported [4,32]. Adding GO and PGO to the PAM hydrogel increased ionic conductivity, but PGO had a much stronger effect on ionic conductivity, increasing its value more than two times higher than the pure PAM hydrogel. Such an outcome can be attributed to the introduction of highly hydrophilic phosphonic acid functional groups onto GO nano-sheets, leading to higher electrolyte storage capacity and greater interaction with ionic moieties in the hydrogel.

The temperature dependence of ionic conductivities of PAM, PAM-GO, and PAM-PGO hydrogels was studied in the range: 20–60 °C in order to understand their ionic conduction mechanism. As shown in Fig. 4, all GPEs show positive temperature-conductivity dependence, following classical Arrhenius behavior, as in Eq. (4) [33]:

$$\ln \sigma = \ln \sigma_0 - E_a/RT \quad (4)$$



**Table 1**  
Comparison of electrochemical performances of different gel polymer electrolytes.

GPE	Cathode	Ionic conductivity (S cm <sup>-1</sup> )	Current density/C rate	Capacity retention (%)	Cycling performance	Ref.
PAM-PGO	MnO <sub>2</sub>	3.1 × 10 <sup>-2</sup> @ 30 °C	0.1 A g <sup>-1</sup>	96	With initial capacity of 240 mAh/g, losing only 4 and 15% of its capacity after 100 and 145 cycles	This work
P(ICZn-AAM) SIHE **	V <sub>2</sub> O <sub>5</sub>	2.15 × 10 <sup>-3</sup>	0.5, 1, 2, 3, 4, and 5 C	N/A	Specific capacity of 271.6 mA h g <sup>-1</sup> over 150 cycles at 2 C; 127.5 mA h g <sup>-1</sup> over 500 cycles at 5 C	[36]
poly [2-(methacryloyloxy) ethyl] dimethyl-(3-sulfopropyl)*	VS <sub>2</sub>	3.2 × 10 <sup>-2</sup>	0.5 A g <sup>-1</sup>	83	stable cycling life of about 3500 h; 89 mA h g <sup>-1</sup>	[39]
CMC/PNiPAAm***	-	1.68 × 10 <sup>-4</sup>	5 mA cm <sup>-2</sup>	N/A	Stable in the charge/discharge cycling for a total of 150 h	[37]
PVA/21 m LiTFSI + 3 m ZnOTf <sub>2</sub>	V <sub>2</sub> O <sub>5</sub>	2.1 × 10 <sup>-3</sup> @20 °C	0.5 A g <sup>-1</sup>	93	600 cycles at 500 mA g <sup>-1</sup> , specific energy of 326 W h kg <sup>-1</sup> at 20 mA g <sup>-1</sup>	[38]

\* poly(vinyl alcohol)/zinc trifluoromethanesulfonate

\*\* iota carrageenan (IC) and acrylamide (AAM) and single-Zn-ion conducting hydrogel electrolyte (SIHE)

\*\*\* carboxymethyl cellulose (CMC)/poly(N-isopropylacrylamide) (PNiPAAm)

where  $\sigma$  is the ionic conductivity,  $\sigma_0$  is the pre-exponential factor,  $E_a$  is activation energy,  $R$  is gas constant, and  $T$  is temperature Kelvin. According to the Arrhenius graph in Fig. 4d, the activation energy for PAM, PAM-GO, and PAM-PGO hydrogels were 10.1, 10.2, and 7.2 KJ/mol K, respectively. This reduction in activation energy of PAM-GO compared to that of PAM and PAM-GO indicates the effect that the PGO additive had in enhancing the ionic conductivity of the PAM-based hydrogels. The presence of PGO nanosheets is seen to result in improved electrolyte retention capacity of the hydrogel and provided additional pathways for ionic conduction. A similar effect has been reported previously [22].

To determine the relative affinity of water against PAM, PAM-GO and PAM-PGO, the binding energies between water molecules and the PAM systems were computed. The results are shown in Fig. 5. The binding energies of the PAM, PAM-GO and PAM-PGO systems binding with water molecules are -14.68, -26.38 and -30.14 kcal/mol, respectively. It indicates that the PAM systems energetically favorably bind with water. In particular, introducing GO additive to PAM can greatly enhance its water affinity, and PGO could further enhance the affinity of PAM with water. In addition, the binding energies between water molecules and GO and PGO were investigated. The binding energies of the GO, PGO and PAM-PGO flakes with water molecules are 731.87, -20.17 and -30.14 kcal/mol (Fig. S2), respectively. Introducing phosphonic acid functional groups can significantly increase the water affinity of the GO flakes. Therefore, the water affinity of PAM and PGO could be enhanced by each other, and they work synergistically toward improved ionic conductivity of the gel electrolyte.

### 3.2.2. Cyclic voltammetry

The electrochemical kinetics of ZIBs with the developed GPEs were analyzed using CV at various scan rates of 0.2, 0.5, 1, 2, and 5 mV/s at 30 °C (Fig. 6a, c, and e). Thus, two cathodic peaks and one anodic peak with a shoulder are revealed in the voltage range of 1 to 1.8 V. Such an outcome is seen to be in agreement with the GCD profile, showing two distinct discharge plateaus and a semi-double staged charge regime at similar voltages. When scan rates are increased for all samples, it is noted that the anodic peaks shift to more positive, and the cathodic peaks shift to more negative potentials due to increased electrochemical polarization. Hence, the relationship between peak current ( $i$ ) and scan rate ( $\nu$ ) can be expressed, as in Eq. (5) [4].

$$i = a\nu^b \quad (5)$$

where  $a$  and  $b$  are adjustable parameters. When the value of  $b$  is increased, the capacitive charge storage in the battery increases. Thus, Eq. (6) becomes:

$$\log(i) = b \cdot \log(\nu) + \log(a) \quad (6)$$

where  $b$  is in the range of 0.5 to 1.0. If the electrochemical process is

ionic diffusion-controlled, the  $b$  value is 0.5 and when the process is completely capacitive-controlled:  $b$  is 1.0. Any value in between shows a combined capacitive and diffusive electrochemical process [34]. In Fig. 6b, d, and f, the  $b$  values for two cathodic peaks and one anodic peak for each GPE are depicted. At the beginning of the discharge process (peak 2), PAM indicates a combined diffusive/capacitive process, exhibiting higher control of the process by ionic diffusion. However, for PAM-GO and PAM-PGO the  $b$  values for the first discharge peaks are 0.8 and 0.76, confirming higher capacitive control, and potentially higher power output. This can be attributed to the higher ionic conductivity of the GPEs [4]. For all GPEs, the first point for peak 2 (scan rate of 0.2 mV/s) was outlier and was not included in the slope calculation. For the second discharge peak (peak 1), PAM shows a purely diffusion-controlled charge storage, while for PAM-GO and PAM-PGO a combined diffusive/capacitive process is observed. The  $b$  values of the anodic peak (peak 3) for PAM, PAM-GO, and PAM-PGO were 0.5, 0.52, and 0.56, signifying that the charging process is mostly controlled by ionic diffusion.

### 3.2.3. Electrochemical performance

A symmetrical Zn/GPE/Zn coin cell was used to investigate the reversibility of zinc plating/stripping in the long term. Thus, the cells were cycled at 0.25 mA/cm<sup>2</sup> up to 0.05 mAh/cm<sup>2</sup> for 1000 cycles (400 h). In Fig. 7a, the cycling profiles of the cells assembled using PAM, PAM-PGO, and the aqueous electrolyte with a glass fiber separator as reference are illustrated. As expected, the cell assembled using the aqueous electrolyte shows the lowest overpotential of around 90 mV at the first and last cycle (no. 1000) due to its high ionic conductivity. Consequently, the overpotential of the cell using PAM as the GPE increased from 125 mV at the start of the test to 152 mV at the last cycle. PAM-PGO revealed a very stable cycling profile up to 400 cycles. Furthermore, adding PGO to PAM decreased the overpotential to 104 mV for the first, and 110 mV for the last cycle. In Fig. 7a, the insert figure depicts the enlarged cycling profile at 200, further confirming the increased ionic conductivity of PAM-PGO and its high interfacial stability with the zinc electrodes [35]. Performance of PAM-PGO, tested at a higher rate and capacity (2.5 and 3.5 mA/cm<sup>2</sup> at 1.0 mAh/cm<sup>2</sup> for 150 h), showed excellent cycling stability. Cycling profiles of Zn/GPE/Zn symmetric cells with PAM-PGO are shown in Fig. S3.

Rate performance was evaluated using coin cells assembled with as prepared GPEs and  $\alpha$ -MnO<sub>2</sub> as the cathode active material. The cells were discharged at 50, 100, 200, 500, 1000, 2000, and 50 mA/g (10 cycles each) and their corresponding capacity was measured. As shown in Fig. 7b, the cell assembled using PAM-PGO showed the best performance compared to those with PAM and PAM-GO as GPE. At 50 mA/g, the cell using PAM-PGO delivered a high capacity of 263 mAh/g, compared to 224 and 236 mAh/g for PAM-GO and PAM, respectively (10th cycle). When the current density increased to 100, 200, and 500 mA/g, the capacity of the PAM-PGO-based cell decreased to 239, 200,

and 139 mAh/g; it was higher than those of the cells assembled using PAM-GO and PAM. However, at very high current densities of 1000 and 2000 mA/g, the cells using all three GPEs signified quite low capacities of around 85 and 50 mAh/g, respectively. After 10 cycles of discharging the cells at 2000 mA/g, the PAM-PGO-based cell revived its initial capacity of 50 mA/g, reaching an even higher discharge capacity of 271 mAh/g. Thus, these results confirm the superiority of PAM-PGO hydrogels compared to PAM and PAM-GO hydrogels to be used as GPEs for ZIBs. In Fig. S4a–c, the GCD profiles of the Zn-MnO<sub>2</sub> batteries with PAM, PAM-GO, and PAM-PGO at various current densities are outlined.

In Fig. 7b, the cycling performance of Zn-MnO<sub>2</sub> cells with various electrolytes at a charge/discharge current density of 100 mA/g along with their coulombic efficiencies during 145 cycles are compared. Moreover, their capacity retentions are shown in Fig. S4d. For all samples, capacity retention was calculated with regards to the 10th cycle. The cell using the aqueous electrolyte exhibited a low initial capacity of 188 mAh/g. After 100 and 145 cycles, the capacity dropped to 166 and 140 mAh/g, showing 90 and 75% capacity retention, respectively. The cell with the PAM electrolyte performed better, reaching 216 mAh/g with about 1% drop after 100 cycles. However, after 145 cycles, capacity decreased to 165 mAh/g, revealing a similar capacity retention of 76% to that of the aqueous electrolyte. The initial capacity of the cells assembled using PAM-GO and PAM-PGO was higher, and their capacity decay pattern was similar. PAM-PGO demonstrated improved capacity retention after 145 cycles. The initial capacity of PAM-GO and PAM-PGO was around 240 mAh/g, dropping to around 230 mAh/g with 96% capacity retention. After 145 cycles, the capacity of the cell with PAM-GO decreased by 20%, reaching 190 mAh/g while the value for the cell with PAM-PGO reached 203 mAh/g, showing 15% capacity decay.

Table 1 shows a comparison of electrochemical performances of the ZIB using PAM-PGO and other ZIBs using different GPEs previously reported. The ionic conductivity of PAM-PGO outperforms most of the reported polymer electrolytes for ZIBs [36–38]. The resulting ZIB also showed reasonably high-capacity retention. In PAM-PGO, fast transport of Zn ions is enabled by the high ionic conductivity, which is advantageous to battery performance. Moreover, it is evident that the incorporation of acidic or basic functional groups into the hydrogel structure can increase the amount of trapped water and the water is seen to host multiple ions. As a result, higher ionic conductivity for GPEs is achieved. Furthermore, the incorporation of acidic groups into the structure of the gel leads to the formation of several hydrogen bonds between the PGO additive and the PAM 3D hydrogel structure, potentially improving the mechanical properties of the gel.

#### 4. Conclusion

Phosphonated graphene oxide was synthesized successfully and used as an additive to PAM hydrogels to be used in ZIBs as GPEs. Compared to PAM (13.8 mS/cm) and PAM-GO (20.8 mS/cm), PAM-PGO hydrogel showed higher ionic conductivity of 31.0 mS/cm at 30 °C, which is attributed to the presence of highly hydrophilic phosphonic acid groups in PGO, due to higher electrolyte absorption and retention capacity. The lower ionic conduction activation energy of PAM-PGO compared to that of PAM and PAM-GO was found to be in accordance with its higher ionic conduction. Using cyclic voltammetry at various scan rates revealed a greater contribution of capacitive charge storage compared to PAM during discharge. Such an outcome denoted a higher power output. Furthermore, the lower overpotential of PAM-PGO than that of PAM, tested in a symmetrical zinc cell using GPE for 400 h, confirmed its higher ionic conductivity and its high interfacial stability with zinc electrodes. In addition, the Zn-MnO<sub>2</sub> batteries assembled using PAM, PAM-GO, and PAM-PGO demonstrated higher capacity and better capacity revival of PAM-PGO-based cells. Finally, the GCD profile of the Zn-MnO<sub>2</sub> cells assembled using various GPEs also signified the superiority of PAM-PGO compared to PAM, PAM-GO, and the aqueous

electrolyte. The result of this study shows better performance of PAM-PGO hydrogels compared to PAM and PAM-GO for use as the solid-state electrolyte in ZIBs.

#### Author contributions

A.A., S.K. and E.A. proposed the research idea. A.A., Y.X. and Y.L. expanded the idea and designed the experiments. A.A. carried out the experiments. S.R. designed and supplied the X-ray tomography cell. H.J. performed DFT calculation and related analysis. V.K.R., I.M., and N.K. carried out X-ray tomography and wrote the mathematical algorithm for the calculation of gel thickness. A.A., Y.X. M.E., R.K., A.S., and S.K. analyzed and discussed the results. A.A. and S.K. prepared the manuscript. E.A. provided extra insight into the structural characterization. All authors commented and reviewed the manuscript.

#### Funding

Thailand Science Research and Innovation Fund Chulalongkorn University (CU\_FRB65\_bcg (6)\_074\_23\_04), The Program Management Unit for Human Resources & Institutional Development, Research and Innovation (B16F640166), and the Energy Storage Cluster, Chulalongkorn University are acknowledged. A.A. thanks Chulalongkorn Academic Advancement into its 2nd Century Project for Postdoctoral Fellowship.

#### Declaration of Competing Interest

The authors declare the following financial interests/personal relationships which may be considered as potential competing interests:

Soorathep Kheawhom reports financial support was provided by The Program Management Unit for Human Resources & Institutional Development, Research and Innovation.

#### Data Availability

Data will be made available on request.

#### Acknowledgments

The authors would also like to thank Dr. Duong Tung Pham for SEM/EDX analysis, Dr. Sarhan Radwan for Raman spectroscopy, and Dr. Ranielle de Oliveira Silva for FTIR spectroscopy.

#### Supplementary materials

Supplementary material associated with this article can be found, in the online version, at doi:10.1016/j.electacta.2022.141365.

#### References

- [1] N. Wang, H. Wan, J. Duan, X. Wang, L. Tao, J. Zhang, H. Wang, A review of zinc-based battery from alkaline to acid, *Mater. Today Adv.* 11 (2021), 100149, <https://doi.org/10.1016/j.mtadv.2021.100149>.
- [2] W. Kao-ian, A.A. Mohamad, W.-R. Liu, R. Pornprasertsuk, S. Siwamogsatham, S. Kheawhom, Stability enhancement of zinc-ion batteries using non-aqueous electrolytes, *Batter. Supercaps* 5 (5) (2022), e202100361, <https://doi.org/10.1002/batt.202100361>.
- [3] W. Kao-ian, M.T. Nguyen, T. Yonezawa, R. Pornprasertsuk, J. Qin, S. Siwamogsatham, S. Kheawhom, Highly stable rechargeable zinc-ion battery using dimethyl sulfoxide electrolyte, *Mater. Today Energy* (2021), 100738, <https://doi.org/10.1016/j.mtener.2021.100738>.
- [4] Y. Quan, M. Chen, W. Zhou, Q. Tian, J. Chen, High-performance anti-freezing flexible Zn-MnO<sub>2</sub> battery based on polyacrylamide/graphene oxide/ethylene glycol gel electrolyte, *Chem.* 8(603) (2020), 10.3389/fchem.2020.00603.
- [5] E.J. Hansen, J. Liu, Materials and structure design for solid-state zinc-ion batteries: a mini-review, *Front. Energy Res.* 8 (2021), <https://doi.org/10.3389/feng.2020.616665>.

- [6] J. Shen, B. Yan, T. Li, Y. Long, N. Li, M. Ye, Study on graphene-oxide-based polyacrylamide composite hydrogels, *Compos. Part A Appl. Sci. Manuf.* 43 (9) (2012) 1476–1481, <https://doi.org/10.1016/j.compositesa.2012.04.006>.
- [7] Z.F. Wang, Z.H. Ruan, Z.X. Liu, Y.K. Wang, Z.J. Tang, H.F. Li, M.S. Zhu, T.F. Hung, J. Liu, Z.C. Shi, C.Y. Zhi, A flexible rechargeable zinc-ion wire-shaped battery with shape memory function, *J. Mater. Chem. A* 6 (18) (2018) 8549–8557, <https://doi.org/10.1039/c8ta01172a>.
- [8] S. Huang, F. Wan, S.S. Bi, J.C. Zhu, Z.Q. Niu, J. Chen, A self-healing integrated all-in-one zinc-ion battery, *Angew. Chem. Int. Ed.* 58 (13) (2019) 4313–4317, <https://doi.org/10.1002/anie.201814653>.
- [9] X.M. Zhu, H.X. Yang, Y.L. Cao, X.P. Ai, Preparation and electrochemical characterization of the alkaline polymer gel electrolyte polymerized from acrylic acid and KOH solution, *Electrochim. Acta* 49 (16) (2004) 2533–2539, <https://doi.org/10.1016/j.electacta.2004.02.008>.
- [10] H.F. Li, Z.X. Liu, G.J. Liang, Y. Huang, Y. Huan, M.S. Zhu, Z.X. Pei, Q. Xue, Z. J. Tang, Y.K. Wang, B.H. Li, C.Y. Zhi, Waterproof and tailorable elastic rechargeable yarn zinc ion batteries by a cross-linked polyacrylamide electrolyte, *ACS Nano* 12 (4) (2018) 3140–3148, <https://doi.org/10.1021/acsnano.7b09003>.
- [11] Y. Huang, M. Zhong, F. Shi, X. Liu, Z. Tang, Y. Wang, Y. Huang, H. Hou, X. Xie, C. Zhi, An intrinsically stretchable and compressible supercapacitor containing a polyacrylamide hydrogel electrolyte, *Angew. Chem. Int. Ed.* 56 (31) (2017) 9141–9145, <https://doi.org/10.1002/anie.201705212>.
- [12] D. Wang, H. Li, Z. Liu, Z. Tang, G. Liang, F. Mo, Q. Yang, L. Ma, C. Zhi, A Nanofibrillated cellulose/polyacrylamide electrolyte-based flexible and sewable high-performance Zn-MnO<sub>2</sub> battery with superior shear resistance, *14(51)* (2018) e1803978. [10.1002/sml.201803978](https://doi.org/10.1002/sml.201803978).
- [13] H. Li, C. Han, Y. Huang, Y. Huang, M. Zhu, Z. Pei, Q. Xue, Z. Wang, Z. Liu, Z. Tang, Y. Wang, F. Kang, B. Li, C. Zhi, An extremely safe and wearable solid-state zinc ion battery based on a hierarchical structured polymer electrolyte, *Energy Environ. Sci.* 11 (4) (2018) 941–951, <https://doi.org/10.1039/C7EE03232C>.
- [14] N. Zhang, F. Cheng, J. Liu, L. Wang, X. Long, X. Liu, F. Li, J. Chen, Rechargeable aqueous zinc-manganese dioxide batteries with high energy and power densities, *Nat. Commun.* 8 (1) (2017) 405, <https://doi.org/10.1038/s41467-017-00467-x>.
- [15] F. Wan, L. Zhang, X. Dai, X. Wang, Z. Niu, J. Chen, Aqueous rechargeable zinc/sodium vanadate batteries with enhanced performance from simultaneous insertion of dual carriers, *9(1)* (2018) 1656. [10.1038/s41467-018-04060-8](https://doi.org/10.1038/s41467-018-04060-8).
- [16] Z. Hou, X. Zhang, X. Li, Y. Zhu, J. Liang, Y. Qian, Surfactant widens the electrochemical window of an aqueous electrolyte for better rechargeable aqueous sodium/zinc battery, *5(2)* (2017) 730–738. [10.1039/C6TA08736A](https://doi.org/10.1039/C6TA08736A).
- [17] C.W. Lee, K. Sathiyarayanan, S.W. Eom, H.S. Kim, M.S. Yun, Novel electrochemical behavior of zinc anodes in zinc/air batteries in the presence of additives, *J. Power Sources* 159 (2) (2006) 1474–1477, <https://doi.org/10.1016/j.jpowsour.2005.11.074>.
- [18] Q. Zhang, Z. Yang, H. Ji, X. Zeng, Y. Tang, D. Sun, H. Wang, Issues and rational design of aqueous electrolyte for Zn-ion batteries, *SusMat* 1 (3) (2021) 432–447, <https://doi.org/10.1002/sus2.20>.
- [19] K. Tang, C. Yuan, Y. Xiong, H. Hu, M. Wu, Inverse-opal-structured hybrids of N, S-codoped-carbon-confined Co<sub>9</sub>S<sub>8</sub> nanoparticles as bifunctional oxygen electrocatalyst for on-chip all-solid-state rechargeable Zn-air batteries, *Appl. Catal. B Environ.* 260 (2020), 118209, <https://doi.org/10.1016/j.apcatb.2019.118209>.
- [20] B. Zhang, Y. Cao, S. Jiang, Z. Li, G. He, H. Wu, Enhanced proton conductivity of Nafion nano-hybrid membrane incorporated with phosphonic acid functionalized graphene oxide at elevated temperature and low humidity, *J. Membr. Sci.* 518 (2016) 243–253, <https://doi.org/10.1016/j.memsci.2016.07.032>.
- [21] A. Cali, Y. Yağızatlı, A. Sahin, İ. Ar, Highly durable phosphonated graphene oxide doped polyvinylidene fluoride (PVDF) composite membranes, *Int. J. Hydrog. Energy* 45 (60) (2020) 35171–35179, <https://doi.org/10.1016/j.ijhydene.2020.01.092>.
- [22] E. Abouzari-Lotf, M. Zakeri, M.M. Nasef, M. Miyake, P. Mozarmnia, N.A. Baziliah, N.F. Emelin, A. Ahmad, Highly durable polybenzimidazole composite membranes with phosphonated graphene oxide for high temperature polymer electrolyte membrane fuel cells, *J. Power Sources* 412 (2019) 238–245, <https://doi.org/10.1016/j.jpowsour.2018.11.057>.
- [23] M. Etesami, E. Abouzari-Lotf, A. Ripin, M. Mahmoud Nasef, T.M. Ting, A. Saharkhiz, A. Ahmad, Phosphonated graphene oxide with high electrocatalytic performance for vanadium redox flow battery, *Int. J. Hydrog. Energy* 43 (1) (2018) 189–197, <https://doi.org/10.1016/j.ijhydene.2017.11.050>.
- [24] M. Zakeri, E. Abouzari-Lotf, M. Miyake, S. Mehdi-pour-Ataei, K. Shameli, Phosphoric acid functionalized graphene oxide: a highly dispersible carbon-based nanocatalyst for the green synthesis of bio-active pyrazoles, *Arab. J. Chem.* 12 (2) (2019) 188–197, <https://doi.org/10.1016/j.arabjc.2017.11.006>.
- [25] D.Y. Putro, M.H. Alfaruqi, S. Islam, S. Kim, S. Park, S. Lee, J.Y. Hwang, Y.K. Sun, J. Kim, Quasi-solid-state zinc-ion battery based on  $\alpha$ -MnO<sub>2</sub> cathode with husk-like morphology, *Electrochim. Acta* 345 (2020), 136189, <https://doi.org/10.1016/j.electacta.2020.136189>.
- [26] J. Moosmann, A. Ershov, V. Weinhardt, T. Baumbach, M.S. Prasad, C. LaBonne, X. Xiao, J. Kashef, R. Hofmann, Time-lapse X-ray phase-contrast microtomography for in vivo imaging and analysis of morphogenesis, *9(2)* (2014) 294–304. [10.1038/nprot.2014.033](https://doi.org/10.1038/nprot.2014.033).
- [27] J. Vlassenbroeck, B. Masschaele, V. Cnudde, M. Dierick, K. Pieters, L. Van Hoorebeke, P. Jacobs, J. Desruets, G. Viggiani, P. Bésuelle, Octopus 8: a high performance tomographic reconstruction package for X-ray tube and synchrotron micro-CT (Eds.). *Advances in X-ray Tomography for Geomaterials*, Wiley-ISTE, 2006, pp. 167–173.
- [28] I.S. Ufimtsev, T.J. Martinez, Quantum chemistry on graphical processing units. 3. Analytical energy gradients, geometry optimization, and first principles molecular dynamics, *J. Chem. Theory Comput.* 5 (10) (2009) 2619–2628, <https://doi.org/10.1021/ct9003004>.
- [29] S. Some, I. Shackery, S.J. Kim, S.C. Jun, Phosphorus-doped graphene oxide layer as a highly efficient flame retardant, *Chem. Eur. J.* 21 (44) (2015) 15480–15485, <https://doi.org/10.1002/chem.201502170>.
- [30] J. Li, Y. Song, Z. Ma, N. Li, S. Niu, Y. Li, Preparation of polyvinyl alcohol graphene oxide phosphonate film and research of thermal stability and mechanical properties, *Ultrason. Sonochem.* 43 (2018) 1–8, <https://doi.org/10.1016/j.ultsonch.2018.01.003>.
- [31] A. Abbasi, S. Hosseini, A. Somwangthanaroj, A.A. Mohamad, S. Kheawhom, Poly(2,6-dimethyl-1,4-phenylene oxide)-based hydroxide exchange separator membranes for zinc-air battery, *Int. J. Mol. Sci.* 20 (15) (2019) 3678, <https://doi.org/10.3390/ijms20153678>.
- [32] Z.F. Liu, C.Y. Zhu, Y.W. Ye, Y.H. Zhang, F. Cheng, H.-R. Li, Synergistic optimization strategy involving sandwich-like MnO<sub>2</sub>@rGO and laponite-modified PAM for high-performance zinc-ion batteries and zinc dendrite suppression, *ACS Appl. Mater. Interfaces* (2022), <https://doi.org/10.1021/acsami.2c02334>.
- [33] K. Sowthari, S.A. Suthanthiraraj, Preparation and properties of a gel polymer electrolyte system based on poly-epsilon-caprolactone containing 1-ethyl-3-methylimidazolium bis(trifluoromethylsulfonyl)imide, *J. Phys. Chem. Solids* 75 (6) (2014) 746–751, <https://doi.org/10.1016/j.jpcs.2014.02.003>.
- [34] Z. Li, S. Ganapathy, Y. Xu, Z. Zhou, M. Sarilar, M. Wagemaker, 2019, Mechanistic insight into the electrochemical performance of Zn/VO<sub>2</sub> batteries with an aqueous ZnSO<sub>4</sub> electrolyte, *9(22)* 1900237. [10.1002/aenm.201900237](https://doi.org/10.1002/aenm.201900237).
- [35] L. Wang, K.W. Huang, J. Chen, J. Zheng, Ultralong cycle stability of aqueous zinc-ion batteries with zinc vanadium oxide cathodes, *5(10)* (2019) eaax4279. [10.1126/sciadv.aax4279](https://doi.org/10.1126/sciadv.aax4279).
- [36] C.Y. Chan, Z. Wang, Y. Li, H. Yu, B. Fei, J.H. Xin, Single-ion conducting double-network hydrogel electrolytes for long cycling zinc-ion batteries, *ACS Appl. Mater. Interfaces* 13 (26) (2021) 30594–30602, <https://doi.org/10.1021/acsami.1c05941>.
- [37] I. Dueramae, M. Okhawilail, P. Kasemsiri, H. Uyama, R. Kita, Properties enhancement of carboxymethyl cellulose with thermo-responsive polymer as solid polymer electrolyte for zinc ion battery, *Sci. Rep.* 10 (1) (2020) 12587, <https://doi.org/10.1038/s41598-020-69521-x>.
- [38] H. Zhang, X. Liu, H. Li, B. Qin, S. Passerini, High-voltage operation of a V<sub>2</sub>O<sub>5</sub> cathode in a concentrated gel polymer electrolyte for high-energy aqueous zinc batteries, *ACS Appl. Mater. Interfaces* 12 (13) (2020) 15305–15312, <https://doi.org/10.1021/acsami.0c02102>.
- [39] K. Leng, G. Li, J. Guo, X. Zhang, A. Wang, X. Liu, J. Luo, A safe polyzwitterionic hydrogel electrolyte for long-life quasi-solid state zinc metal batteries, *Adv. Funct. Mater.* 30 (23) (2020), 2001317, <https://doi.org/10.1002/adfm.202001317>.